Remote Sensing Applications: Society and Environment 32 (2023) 101022

Contents lists available at ScienceDirect

Remote Sensing Applications: Society and Environment

journal homepage: www.elsevier.com/locate/rsase

Identification of pegmatites zones in Muiane and Naipa (Mozambique) from Sentinel-2 images, using band combinations, band ratios, PCA and supervised classification

Ubaldo Gemusse [a, b, c], Joana Cardoso-Fernandes [b, c], Alexandre Lima [b, c], Ana Teodoro [b, c, *]

[a] Department of Sciences, Faculty of Science and Technology, Licungo University, PO Box 2025, Beira, Mozambique
[b] Institute of Earth Sciences (Porto Pole), Porto, Portugal
[c] Department of Geosciences, Environment and Land Planning, Faculty of Sciences, University of Porto, 4169-007, Porto, Portugal

ARTICLE INFO

Keywords:
LCT pegmatites
Maximum likelihood
Support vector machines
Radial basis function
Supervised classification
Sentinel-2a
Reflectance spectroscopy

ABSTRACT

Remote sensing has been widely used in Geological Sciences for different applications, such as to identify geological and mineralogical objects and surface alteration changes. This study aimed to analyze the Sentinel-2 potential to detect pegmatite bodies and associated alteration zones in Muiane and Naipa in Mozambique. Different remote sensing techniques were applied to a Sentinel-2 image: RGB combinations, band ratios, principal component analysis (PCA), and supervised image classification algorithms such as the Maximum Likelihood Classifier (MLC) and Support Vector Machine (SVM). MLC was used as a benchmark classifier to evaluate the performance of SVM because MLC is the predominant algorithm employed in remote sensing classification studies. For that, several statistical metrics based on the confusion matrices were computed, namely accuracy, Kappa index, precision, recall, and f-score, among others. This study allows identifying the location of pegmatites by direct identification and segregating between hydrothermally altered zones and non-altered areas through remote sensing data/techniques, supported by field data. The field campaigns allowed for validating the results obtained and verifying the pegmatites identified using Sentinel-2 data that were not previously mapped. Moreover, reflectance spectroscopy studies in the laboratory were conducted on the samples collected in the field campaigns allow to validate the adequacy of the methodology proposed in this study. The results show that the precise identification of pegmatite targets requires a high spatial resolution such as Sentinel-2 images. Thus, with the integration of high spatial and spectral resolution data, a potential level of precision and accuracy can be achieved in the study areas.

Abbreviations

CL	Lurio granulitic belt
DOS-1	Dark Object Subtraction

* Corresponding author. Department of Geosciences, Environment and Land Planning, Faculty of Sciences, University of Porto, 4169-007 Porto, Portugal.
E-mail address: amteodor@fc.up.pt (A. Teodoro).

https://doi.org/10.1016/j.rsase.2023.101022
Received 13 April 2023; Received in revised form 16 June 2023; Accepted 26 June 2023
Available online 4 July 2023

FCC	False Color Composite
FN	False Negatives
FNR	False negative rate
FP	False Positives
FPR	False positive rate
LCT	Lithium, Cesium, Tantalum
Li	Lithium
MLC	Maximum Likelihood Classifier
MNF	Minimum noise fraction
NDVI	Normalized Difference Vegetation Index
NYF	Niobium, Yttrium, Fluorine
PA	Producer's accuracy
PC	Principal Component
PCA	Principal component analysis
RBF	Radial basis function
RGB	Red, Green, Blue
SAM	Spectral Angle Mapper
SCP	Semi-Automatic Classification Plugin
SVM	Support Vector Machine
SWIR	Shortwave infrared
TN	True Negatives
TOA	Top of the atmosphere reflectance
TP	True Positives
TPR	True positive rate
UA	User's accuracy
VNIR	Visible and near-infrared

1. Introduction

There are numerous studies concerning remote sensing applied to geosciences (Sabins 1999; Delacourt et al., 2005; Govil et al., 2018; Saibi et al., 2018; Jolie et al., 2019; Cardoso-Fernandes et al., 2020a, 2020b; Didero et al., 2020; Gopinathan et al., 2020). The potential of satellite data for mineral exploration has been evaluated for decades for geological and mineralogical identification in distinct deposit types (Sabins 1999; Ghulam et al., 2010; Yousefi et al., 2018; Adiri et al., 2020; Salehi & Tangestani, 2020). In remote sensing image processing, target identification depends on the way that different materials interact in various manners in each band of the electromagnetic spectrum (Sivakumar et al., 2004; Xie et al., 2008; Jensen 2009; Aqeel et al., 2011).

More recently, the use of remote sensing data for Lithium (Li) detection was reviewed, with studies concerning either pegmatite or brine identification (Cardoso-Fernandes et al., 2020a). Cardoso-Fernandes et al. (2019) used classical image processing techniques such as RGB (red, green, blue) combinations, band ratios, and principal component analysis (PCA) to directly discriminate the Li-pegmatites from the metasedimentary host rocks in the Iberian Peninsula (Fregeneda-Almendra), although the results showed that the use of thermal bands can be crucial for this discrimination. The same authors also tried to identify hydrothermal alteration associated with the pegmatites, but the results did not show evidence of a large extent of alteration. Taking advantage of the Sentinel-2 spatial resolution, essential when the pegmatite bodies of the Fregeneda-Almendra area only reach up to 30 m of lateral extension, Cardoso-Fernandes et al. (2020b) tried to use more powerful techniques, namely machine learning algorithms, to overcome the shortness of Sentinel-2 lacking thermal bands and discriminate the pegmatites from their host rocks. Morsli et al. (2021) utilized spectroradiometric measurements of the pegmatite and other field lithologies to compare their spectral signature and propose new RGB combinations and band ratios, that alongside PCA and minimum noise fraction (MNF) allowed mapping pegmatite veins in the Central Anti-Atlas (Morocco) using ASTER data. Mashkoor et al. (2022) also proposed new band ratios for ASTER to identify Li-minerals and compared the results of False Color Composite (FCC), band ratio, and supervised classification with Spectral Angle Mapper (SAM) algorithm for ASTER, Landsat-8 OLI/TIRS and Sentinel 2 MSI data. In general, the best results were obtained with ASTER data and the most suitable approaches to identify pegmatites in the Konar Province (Eastern Afghanistan) were band ratios and SAM techniques.

The work of Booysen et al. (2022) proved that new technologies such as hyperspectral imaging and machine learning methods can accurately identify the distribution of Li-minerals either in outcrops or drill-cores in pegmatites at Uis (Namibia). In fact, spectroradiometric studies of Li-minerals and a careful interpretation of the obtained spectra provided important insights for exploration, namely that using the wavelength region covered by most satellite sensors (350–2500 nm), spodumene and petalite can only be indirectly identified since their spectra are dominated by features of alteration minerals such as clays, and that effect of alteration paragenesis is crucial in the spectral behavior of both minerals with the clay-related absorption depths decreasing with higher Li content (Cardoso-Fernandes et al., 2021b). Thus, the authors leave an open question: if such minerals could be indirectly detected in areas where clay alteration from other lithologies is prevalent (for example in tropical conditions).

All previously mentioned works concern the detection of LCT (lithium, cesium, tantalum) pegmatites, but there is another family, the NYF (niobium yttrium, fluorine) that is also enriched in raw materials critical for the energy transition (Černý & Ercit, 2005). That is why the current H2020 GREENPEG project (https://www.greenpeg.eu/) aims to develop an exploration toolset, that includes satellite- and drone-based remote sensing, for the identification of both NYF and LCT pegmatites (Müller et al., 2022). Preliminary results show that machine learning algorithms can identify NYF pegmatites in the Tysfjord region (Norway), outperforming classical image processing techniques (Teodoro et al., 2021; Müller et al., 2022; Santos et al., 2022).

The region under study, Alto Ligonha (Mozambique), provides hydrothermal alteration (Neiva & Gomes, 2012) and has unique physical geographical features, such as a tropical climate causing pegmatite alteration, making the Alto Ligonha pegmatites more altered than the bodies in other pegmatite fields in Mozambique. Thus, converging with the idea that primary minerals are intensely weathered (Neiva & Gomes, 2012; Dolui et al., 2016; Chen et al., 2020). Spectral identification of potential areas of hydrothermal alteration minerals is a common application of remote sensing to mineral exploration (Rajesh 2004; Blokoi and Poormirzaee 2009; Sadek et al., 2013; Mahboob et al., 2019; Salehi & Tangestani, 2020; Frutuoso et al., 2021). This is particularly important since previous research works concern areas with distinct characteristics, namely Mediterranean, Polar, Semi-arid, and Temperate climates, for example.

For this work, a Sentinel-2 image was analyzed. The application of Sentinel-2A for geological remote sensing can be found in several studies (van der Meer et al., 2014; van der Werff and van der Meer 2016; Fal et al., 2019; Adiri et al., 2020). Sentinel-2 images have already been proven to be efficient in pegmatite prospecting (Cardoso-Fernandes et al., 2020b; Santos et al., 2019). In general, each type of rock with its characteristic rock-forming minerals has its own reflectance signature, and thus, by using remote sensing techniques, the different rock types in a particular area can be discriminated based on their reflectance characteristics (Riley and Hecker 2013; Corumluoglu et al., 2015; Hassan and Ramadan 2015). That is why reflectance spectroscopy studies were used as a complement to satellite image processing.

Taking this into account, this study aims to evaluate the potential of Sentinel-2 images to detect pegmatites and related alteration zones in the Muiane and Naipa regions, characterized by differentiated conditions (climate, mineralogy of pegmatite, overall geological context), through RGB band combinations and rationing, PCA and supervised classification considering Support Vector Machine (SVM) and Maximum Likelihood (MLC). The choice of supervised classification algorithms was based on theoretical background: (i) machine learning algorithms have demonstrated a great capability of dealing to model complex class signatures in distinct remote sensing studies; (ii) machine learning algorithms usually outperform traditional parametric classifiers in identical classification tasks; (iii) among the available machine learning algorithms, SVM is more robust to deal with smaller and imbalanced datasets; and (iv) MLC was employed as a baseline classifier to compare the performance of SVM since MLC is the most commonly used algorithm for remote-sensing classification approaches (Mountrakis et al., 2011; Yu et al. 2012, 2014; Rodriguez-Galiano et al., 2015; Noi and Kappas 2017; Maxwell et al., 2018; Cardoso-Fernandes et al., 2020b; De Luca et al., 2022; Valdivieso-Ros et al., 2023).

Two methodological approaches were employed for this purpose: (i) application of literature-available methods and algorithms designed exclusively for Li-pegmatite detection or hydrothermal alteration mapping, and (ii) self-propose and improve the same techniques for general pegmatite (*sensu lato*) detection. Therefore, with this study, we do not aim to differentiate between LCT and NYF pegmatites. Several minerals are common to both pegmatite families, namely albite, quartz, and tourmaline. The results of the self-proposed methods were then confronted with the ones obtained with pre-existing methods. The validation was conducted using ground truth samples, and the geological map at a 1/250,000 scale, which was compared with the final classification maps at a scale of 1/100,000. The samples collected during the field validation were analyzed through reflectance spectroscopy for laboratory verification of the methods employed. Ultimately, this research tries to answer if remote sensing techniques can be used to detect pegmatites even in regions where intense alteration occurs in tropical conditions. The refined algorithms developed in this study for pegmatite exploration and their respective performance were extensively compared against existing approaches. The results highlight the success of the new and self-proposed algorithms in pegmatite identification, with the delineation of new exploration targets. Thus, this research is of high relevance in the context of pegmatite exploration and the new findings will aid the development of future practical applications. Moreover, the results represent a great contribution to the geological knowledge of Mozambique and to pegmatite exploration in Africa.

2. Study area

In the Alto Ligonha zone, minerals from the LCT and NYF pegmatite families occur, although the NYF pegmatites predominate in the Rio Licungo pegmatite field than in the study areas of Muaine and Naipa (Černý & Ercit, 2005; Bradley and McCauley 2016; Gomes et al., 2008). Economically, the pegmatites of this region are important because they are the source of colored gemstones such as polychrome tourmalines; topaz; colored varieties of beryl such as aquamarine, emerald, and morganite; amazonite (a green variety of microcline); columbite–tantalite; colored spodumene (a Li-bearing mineral) crystals such as kunzite and hiddenite (a rare green gem variety of spodumene); and an impressive number of collectable mineral species among oxides, phosphates, and silicate minerals (Cronwright 2005; Council for Geoscience, 2007; Gemusse et al., 2018).

Muiane and Naipa are located in the Gile district in the Zambezia province (Central Mozambique) (Fig. 1). The Gile district is bordered to the north by the Murrupula district (Nampula Province), across the river Ligonha, to the south by the Pebane district (Zambezia Province), to the east by the Moma district (Nampula Province), to the west by the Molocué district (Zambezia Province), and to the Southwest by the Ile district (Zambezia Province). Access to this area is extremely precarious (Gemusse et al., 2018).

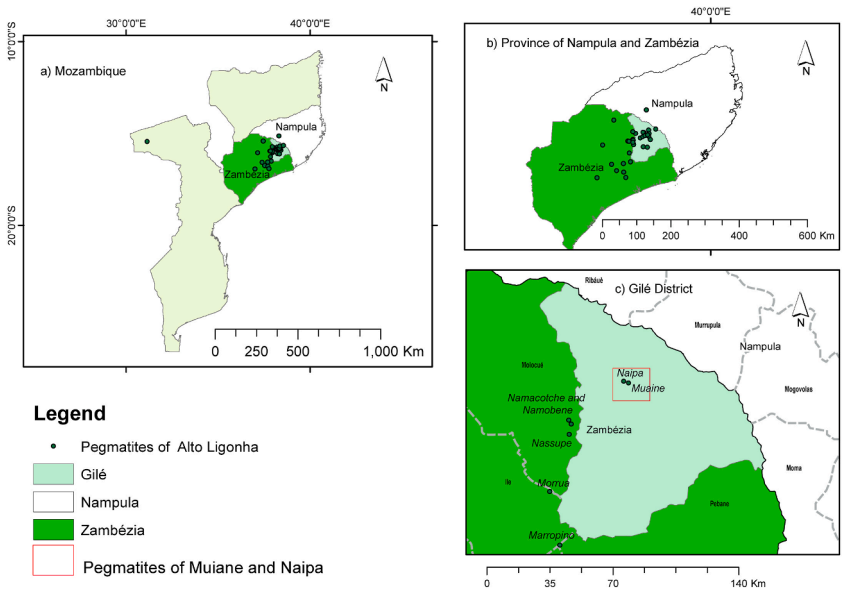

Fig. 1. Location of the Naipa and Muiane pegmatites in the Gilé district (c) of the Zambezia and Nampula Province (b), Mozambique (a). The border between the Zambezia and Nampula Provinces is defined by the course of the Ligonha River.

A considerable number of principal streets in the zone are currently being restored with financing from foreign aid organizations and in the framework of governmental rehabilitation projects that aim at improving the economy (MAE 2005; Gemusse et al., 2019). Taking this into account, remote sensing approaches are extremely helpful to map and detect pegmatites in this area.

This territory is dominated by Mesoproterozoic gneiss of a medium to high metamorphic degree intruded by Pan-African granites (450–530 Ma) and pegmatites (~430–470 Ma) (Abdelsalam et al., 2002; Bingen et al., 2009; Neiva & Gomes, 2010; Neiva & Gomes, 2012). These rocks belong to the Nampula complex, a tectonostratigraphic division of the Mozambique belt, which is located in the south of the Lurio granulitic belt (CL; Fig. 2) (Macey et al., 2006; Boyd et al., 2010; Jacobs et al., 2012).

The Naipa granitic pegmatite is located in Alto Ligonha (Mozambique) and belongs to the LCT pegmatite family (Cronwright 2005; Neiva & Gomes, 2012). Similar lithological characteristics are observed in the Muiane region, where distinct LCT pegmatites suffered from metasomatism, prompting the development of various clay minerals. Regardless, the original pegmatite paragenesis is often difficult to identify due to the intense kaolinization (as a result of supergene alteration and weathering) as well as due to the overprint of hydrothermal–metasomatic alteration (Silva et al., 2009; Bradley et al., 2010). Often, pegmatites from the lepidolite, spo-

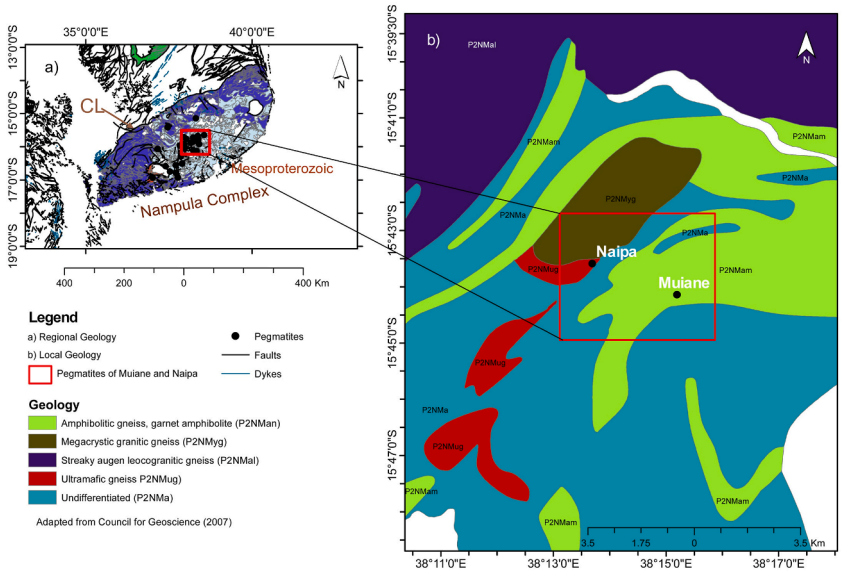

Fig. 2. Regional (a) and local (b) geological map showing the Nampula complex, delimited to NE by the Lurio granulitic belt (CL.

dumene, and elbaite (tourmaline) subtypes can coexist (Quemeneur and Laganche 1999; Černý & Ercit, 2005; Neiva & Gomes, 2012; Gemusse et al., 2019).

In terms of dispersion, the pegmatites occur as dispersed dykes. In the case of the Muiane region, the largest exposed pegmatite is a lenticular body trending NE-SW, dipping 25° to SE, with a lateral extension that can vary between 50 and 110 m (Barros and Vicente 1963). Drilling studies have discovered other parallel bodies with a maximum of 1 km of extension and 400 m of width (Naude and Sperinck 2009). In the Naipa region, the pegmatites form a zoned granitic group, with tourmaline crystals reaching up to 70 cm (Neiva & Gomes, 2012). These pegmatites are structurally complex with evidence of fractionation, with smaller apical extensions emanating from pegmatitic masses of large dimensions, with a lateral extension of up to 30 m (Gomes, 2003). The first field campaign that took place before the remote sensing studies, in the year 2017, allowed the collection of reference samples from the mapped pegmatites of Muiane and Naipa (Fig. 3). The reference samples collected were used for laboratory reflectance studies, specifically to obtain the spectral signature of several pegmatite minerals (see section 4.5). The recognizance campaign also allowed the identification of important heaps of lepidolite and quartz concentrates (Fig. 3) near the premises of the existing pegmatite exploitations, since, at the time, the pegmatites were only exploited for columbite–tantalite minerals and gemstones.

In the proximity of the Muiane and Naipa regions, there are other mapped pegmatites called Namobene, Namacotche, and Nassupe that were not used for algorithm training but instead for validation.

3. Data and image pre-processing

The Level 1-C cloud-free Sentinel-2 imagery covering the study area was acquired on October 10, 2019. The projection is Universal Transverse Mercator zone 37 S, WGS84 datum.

Fig. 4 shows the detailed workflow followed in this study. The Semi-Automatic Classification Plugin (SCP) (Congedo, 2016) for QGIS software was employed for image download and pre-processing, namely: (i) conversion of digital numbers to top of the atmosphere reflectance (TOA) and (ii) atmospheric correction through the Dark Object Subtraction (DOS-1) algorithm (Chavez, 1996). All Sentinel-2 bands were resampled to the same spatial resolution (10 m). SCP under QGIS was also used for the definition of the classification inputs (training areas). To aid in the selection of the training areas, the Normalized Difference Vegetation Index (NDVI) was computed. After the pre-processing stage, the supervised classification was achieved using ENVI software (see Section 4).

4. Methodology

Classical remote sensing methods applied in geological exploration include RGB combinations, band ratios, and PCA, among others (Loughlin 1991; Pour and Hashim 2015; Yousefi et al., 2018; El-leil et al., 2019; Rawashdeh and Hamzah 2020). For all these methods, routine histogram tools (such as stretching) were employed in QGIS as a routine process to improve visualization.

This section aims at describing the image processing methods employed in this work to achieve pegmatite detection. As previously mentioned, two methodological approaches were employed. First, the RGB combinations and selective PCA subsets available in the literature for Li-pegmatite detection were applied to the Alto Ligonha region for targeting pegmatites. Also, known techniques for hydrothermal alteration mapping were employed to identify alteration zones related to existing pegmatites (Hu et al., 2018). Secondly, new RGB, ratios, and PCA combinations were proposed, and supervised image classification algorithms, namely SVM and MLC, were employed to identify target areas for pegmatite exploration (*sensu lato*). Therefore, both barren and Li-mineralized pegmatites should be detected. Both band combinations, band ratios, and PCA were employed using SCP.

Fig. 3. Lepidolite heap containing minor albite with few high grades of microlite from the Naipa pegmatite (2017). Lepidolite was concentrated at the time in tailings since only gemstones and columbite-tantalite were economically exploited. The purple color in the boulders is indicative of the presence of lepidolite. Reference samples were collected at this site. (For interpretation of the references to color in this figure legend, the reader is referred to the Web version of this article.)

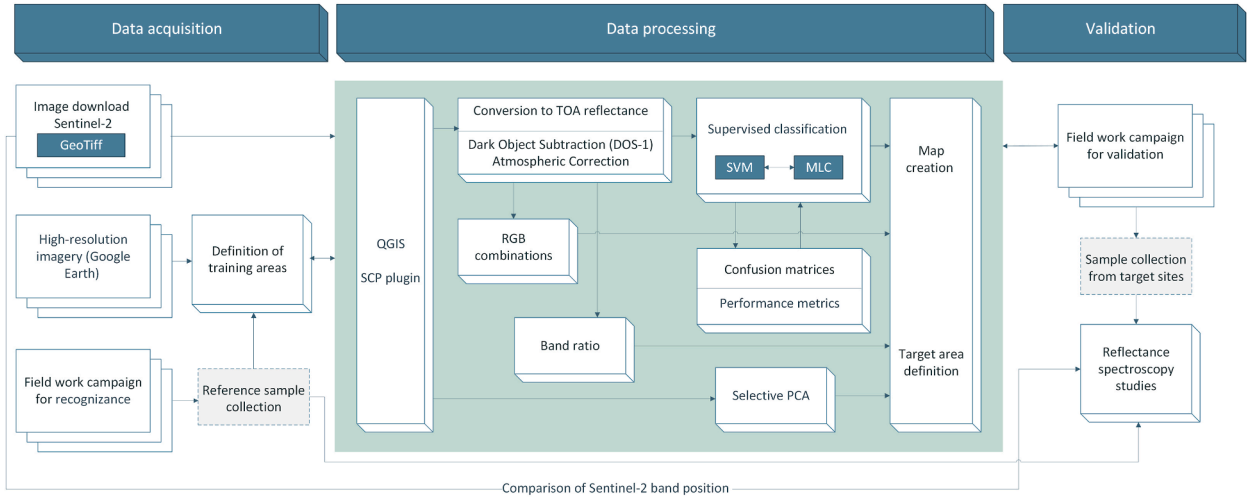

Fig. 4. Workflow illustrating the data acquisition and processing steps followed in the study.

4.1. RGB combinations

To distinguish potential regions of interest for pegmatite exploration, distinctive RGB combinations were tested in this study (Manuel et al., 2017; Santos et al., 2019; Cardoso-Fernandes et al., 2020a), including the Sentinel-2A (3-2-12) combination suggested for the detection of Li-bearing pegmatites in Iberia. Additionally, the combination (3-11-12) was self-proposed in this work through an iterative process for pegmatite prospecting, since some of the combinations, available in the literature for other areas and others that were also self-proposed, did not work in these case studies, namely combinations (2-11-12), (3-2-12), (2-4-11) and (2-7-12).

4.2. Principal component analysis (PCA)

PCA is considered one of the most valuable techniques in digital image processing and a method of statistical analysis that can improve the interpretation of multispectral data (Çorumluoğlu and Vural 2013). It is a multivariate ranking technique that allows for decreasing the dimensionality of the data (Loughlin 1991; Ćfosta et al., 2003; Lu et al., 2004).

Selective PCA was employed in the selected band subsets to identify hydrothermal alteration minerals as suggested by Hu et al. (2018), as well as to map Li-bearing pegmatites (Cardoso-Fernandes et al., 2019) (see Table 1). A new PCA combination was self-proposed for pegmatite detection based on available reference spectra of common pegmatite minerals in the spectral databases provided by the ENVI software (Table 1). The goal was to compare with literature results to assess the most adequate combination for these particular case studies.

4.3. Band ratios

This technique is an excellent option for geological prospecting due to its simplicity to delineate targets with a research interest, by enhancing the spectral behavior of different targets where one spectral band is inversely proportional to another band (Sabins, 1999). For this purpose, the band with the highest reflectance should be divided by the band with the lowest reflectance (usually absorption zones). For this work, band ratios 2/11 and 7/11 were proposed.

4.4. Supervised classification

Distinct methodologies, such as machine learning classifiers like SVM or parametric algorithms like MLC, can be employed to achieve supervised image classification (Huang et al., 2002; Mondal et al., 2012; Chaudhari et al., 2015; Gemusse et al., 2019).

The SVM corresponds to a nonparametric computational learning technique (Vapnik and Lerner 1963; Vapnik 2000; Mountrakis et al., 2011; Gonzalez-Abril et al., 2014; Lewes 2015). To solve nonlinear problems with SVM, different kernel functions can be employed, such as (i) linear, (ii) quadratic, (iii) polynomial, and (iv) radial basis function (RBF). The RBF has shown efficacy in the optimal separation of classes (Gaspar et al., 2012; Martins et al., 2016; Khan et al., 2017) and was therefore chosen in this study. The penalty value (C) and kernel parameter width (γ) are the two parameters of the RBF kernel. In this work, they were set to 100 and 0.167, respectively (ENVI User's Guide, 2009; Petropoulos et al., 2012).

Table 1
Band subsets for selective PCA and respective target processed minerals.

Satellite	PCA	Target	Source
Sentinel 2	2, 8 A, 11, 12	Hydrothermally altered rocks	(Hu et al., 2018)
Sentinel 2	2,3,8,11	Li-bearing pegmatites	(Cardoso-Fernandes et al., 2019; Santos et al., 2019)
Sentinel 2	3,8	Li-bearing pegmatites	(Cardoso-Fernandes et al., 2019; Santos et al., 2019)
Sentinel 2	4,6	Pegmatites	Self-proposed

On the other hand, MLC assumes a Gaussian distribution of the data, and for each unknown pixel, the probability of membership to each class is calculated and the pixel is assigned to the class corresponding to the maximum probability (Richards and Jia 1986; Jia et al., 2014; Lillesand et al., 2015; Long et al., 2016).

A training sample file was created with only four classes: (i) pegmatite class, which is the fusion of many pegmatites in each of the pilot zones of research; (ii) water bodies, which correspond to swamps and accumulation wells, (iii) a mixture of exposed soil (bare or unprotected soil) and housing zones (which correspond to the areas of buildings and housing); and finally, (iv) vegetation, including both arboreal and herbaceous species. These classes were defined with the help of available high-resolution imagery (Google Earth) and field surveys (first field campaign, described in Section 2). Other lithologies were not included as classes in the supervised classification because the land cover does not always correspond with lithological outcrops, mostly because some outcrops are covered by vegetation as evidenced by the NDVI. The impact of vegetation coverage on lithological mapping has been assessed in the literature (Grebby et al., 2014). The definition of the training classes and regions of interest was an iterative process that included class separability analysis through the computation of spectral distances in SCP. To evaluate the classification accuracy, the confusion matrices are presented for each algorithm, and the associated statistics were computed (Table 2), namely the Kappa index, the producer's accuracy (PA); user's accuracy (UA); precision; recall, also known as sensitivity or true positive rate (TPR); F-score; false positive rate (FPR); specificity; and false negative rate (FNR) (Congalton 1991; Congalton and Green 2009; ENVI User's Guide, 2009; Sokolova and Lapalme 2009). Moreover, the quality of the classification can be assessed in two ways: (i) by averaging the same measures calculated for each class (macro-averaging), where all classes are treated equally; or (ii) by counting the sums of the True Positives (TP), True Negatives (TN), False Negatives (FN), and False Positives (FP) and calculating the respective performance measure (micro-averaging), where equal weight is given to each sample, favoring bigger classes (Sokolova and Lapalme 2009).

4.5. Field validation and reflectance spectroscopy

After the application of the aforementioned image processing methods, second field validation was conducted in the year of 2019 in the selected regions of interest. Whenever possible, the validation was conducted by members of the research team. However, in some cases, validation was performed by an external team as part of the mining and sales report ordered by the Tantalum Mineração e Prospecção Limitada exploration company (Gemusse et al., 2021). Hand samples were collected at the validation sites for further reflectance spectroscopy studies, at the Faculty of Sciences of the University of Porto, together with the samples collected in the first fieldwork (recognizance campaign). The spectral measurements were performed in a dark environment with an ASD FieldSpec 4 spectrometer with standard resolution covering the 350–2500 nm region, employing a contact probe with an internal halogen lamp and a spot size of 10 nm. Several spots were analyzed for every sample. In each spot, five measurements (consisting of 40 scans) were averaged into a final spectrum to increase the signal-to-noise ratio. White reference calibration was made using a Spectralon (Labsphere) plate. The equipment characteristics and measurement protocol are described in detail in previous works (Cardoso-Fernandes et al., 2021a, 2021b).

5. Results and discussion

The results for selective PCA, RGB band combinations, and supervised classification are presented in this section.

Table 2
Employed formulas for statistical measures used to evaluate the classification results (following the work of Sokolova and Lapalme 2009 and ENVI User's Guide, 2009).

Measure	Formula	Measure	Formula
Accuracy (micro)	$\frac{\sum_{i=1}^{l} TP_i}{\sum_{i=1}^{l} G_i}$	Average Accuracy (macro)	$\sum_{i=1}^{l} \frac{\frac{TP_i+TN_i}{TP_i+FN_i+FP_i+TN_i}}{l}$
PA_i	$\frac{m_{i,i}}{G_i}$	UA_i	$\frac{m_{i,i}}{C_i}$
Precision $_{micro}$	$\frac{\sum_{i=1}^{l} TP_i}{\sum_{i=1}^{l} TP_i+FP_i}$	Precision $_{macro}$	$\sum_{i=1}^{l} \frac{\frac{TP_i}{TP_i+FP_i}}{l}$
Recall $_{micro}$	$\frac{\sum_{i=1}^{l} TP_i}{\sum_{i=1}^{l} TP_i+FN_i}$	Recall $_{macro}$	$\sum_{i=1}^{l} \frac{\frac{TP_i}{TP_i+FN_i}}{l}$
F-score $_{micro}$	$2 \times \frac{Precision_{micro} \times Recall_{micro}}{Precision_{micro}+Recall_{micro}}$	F-score $_{macro}$	$2 \times \frac{Precision_{macro} \times Recall_{macro}}{Precision_{macro}+Recall_{macro}}$
FPR $_{micro}$	$\frac{\sum_{i=1}^{l} FP_i}{\sum_{i=1}^{l} FP_i+TN_i}$	FPR $_{macro}$	$\sum_{i=1}^{l} \frac{\frac{FP_i}{FP_i+TN_i}}{l}$
FNR $_{micro}$	$\frac{\sum_{i=1}^{l} FN_i}{\sum_{i=1}^{l} FN_i+TP_i}$	FNR $_{macro}$	$\sum_{i=1}^{l} \frac{\frac{FN_i}{FN_i+TP_i}}{l}$
Specificity $_{micro}$	$\frac{\sum_{i=1}^{l} TN_i}{\sum_{i=1}^{l} TN_i+FP_i}$	Specificity $_{macro}$	$\sum_{i=1}^{l} \frac{\frac{TN_i}{TN_i+FP_i}}{l}$
Kappa index	$\frac{N\sum_{i=1}^{l} m_{i,i}-\sum_{i=1}^{l}(G_i C_i)}{N^2-\sum_{i=1}^{l}(G_i C_i)}$		

*PA – producer's accuracy; UA – user's accuracy; TPR – true positive rate; FPR – false positive rate; FNR – false negative rate; TP – true positives; TN – true negatives; FN – false negatives; FP – False Positives; i – class number; l – total number of classes; N – total number of classified values compared to truth values; $m_{i,i}$ – number of values belonging to the truth class i that have also been classified as class i (i.e., values found along the diagonal of the confusion matrix); C_i – total number of predicted values belonging to class i; G_i – total number of truth values belonging to class i.

5.1. PCA

From the subsets applied for selective PCA (Table 1), only those that achieved the best results are presented. The best outcome was achieved using the two-band subset for Sentinel-2 bands 3 and 8, with the second principal component (-PC2) highlighting in bright pixels both the Muiane and Naipa mines, as well as other pegmatite occurrences.

For the Muiane and Naipa target areas, PCA was the most proficient strategy for pegmatite detection. These results are in line with the work of Santos et al. (2019), where PCA showed a better performance compared to other classical image processing techniques. Moreover, the same subset for selective PCA allowed identifying new territories where different pegmatites occur.

Fig. 5 represents the selected PC after applying PCA to bands 4 and 6, displaying greenfield target areas for pegmatite exploration in white pixels. Nonetheless, it is noticeable some misclassifications with dirt roads also displayed in white pixels as seen in Fig. 5b. This spectral similarity can be due to similar mineral assemblages, namely clay minerals, that are present in both pegmatites and soils/dirt roads. Fig. 5b corresponds to the training areas of Muiane and Naipa, while (a1) and (a2) to the Namacotche and Nassupe pegmatites, respectively (in a close-up view of Fig. 5a), where Li minerals and LCT pegmatites are known to occur (Council for Geoscience, 2007; Gomes et al., 2008). Fig. 5 (b1) corresponds to a new exploration field named by the authors as Muiane II, where pegmatites were detected through remote sensing. During the field validation of the Muiane II site, the pegmatites detected through remote sensing were identified as unexploited Li-bearing pegmatite dikes intruding mainly granites and gneisses, with visible Kunzite (spodumene) gemstones, and lepidolite. At the time of field validation in 2019, it was possible to find some artisanal and unlicensed exploration works for gold, tantalite, and tourmaline gems (locality known as "*garimpo*"). None of these works were related to lithium exploration. Due to difficulties in getting access to the property, field validation was conducted by a third party (Gemusse et al., 2021). Nonetheless, these pegmatite occurrences were unmapped until field validation and indicate that Muiane II is a possible new Li-pegmatite prospect area. Thus, the self-proposed PCA with bands 4 and 6 represents a major contribution to future pegmatite exploration approaches (with four out of five known pegmatites identified with confidence).

The results of selective PCA on Sentinel-2 bands 3 and 8, with negated PC2 displaying target areas for exploration in white pixels (not shown in this work). The results are similar to the ones of the self-proposed band subset (4 and 6 bands), although the performance in the Namobene and Nassupe areas is higher. Nonetheless, the mentioned subset for PCA allowed identifying (i) the training areas of Muiane and Naipa, (ii) the validation sites of Namobene and Nassupe, and (iii) the new prospect area, previously identified, the Muiane II site.

Finally, the four-band subset (Fig. 6) available in the literature to identify areas of hydrothermal alteration (i.e., where hydroxyl-bearing minerals occur) allowed to identify the Muiane, Muiane II, and Naipa areas (b; b1), while the occurrence of alteration minerals is more dispersed in the validation sites of Namobene (a), Namacotche (a1) and Nassupe (a2). Thus, Fig. 6 represents the resultant PC after applying PCA to bands 2, 8 A, 11, and 12.

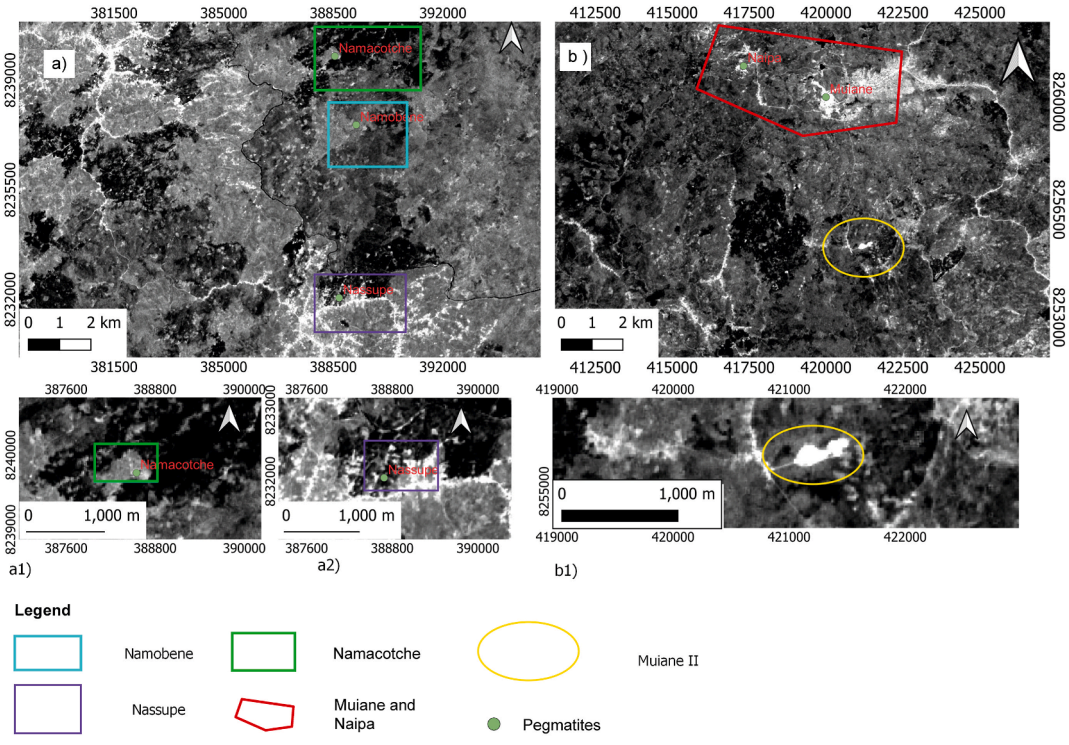

Fig. 5. Mosaic result of the self-proposed selective PCA on Sentinel-2 bands 4 and 6 (resultant PC), allowing the identification of the training areas of Muiane and Naipa (b), the validation site of Namacotche (a1), and the new prospect area of Muiane II (b1).

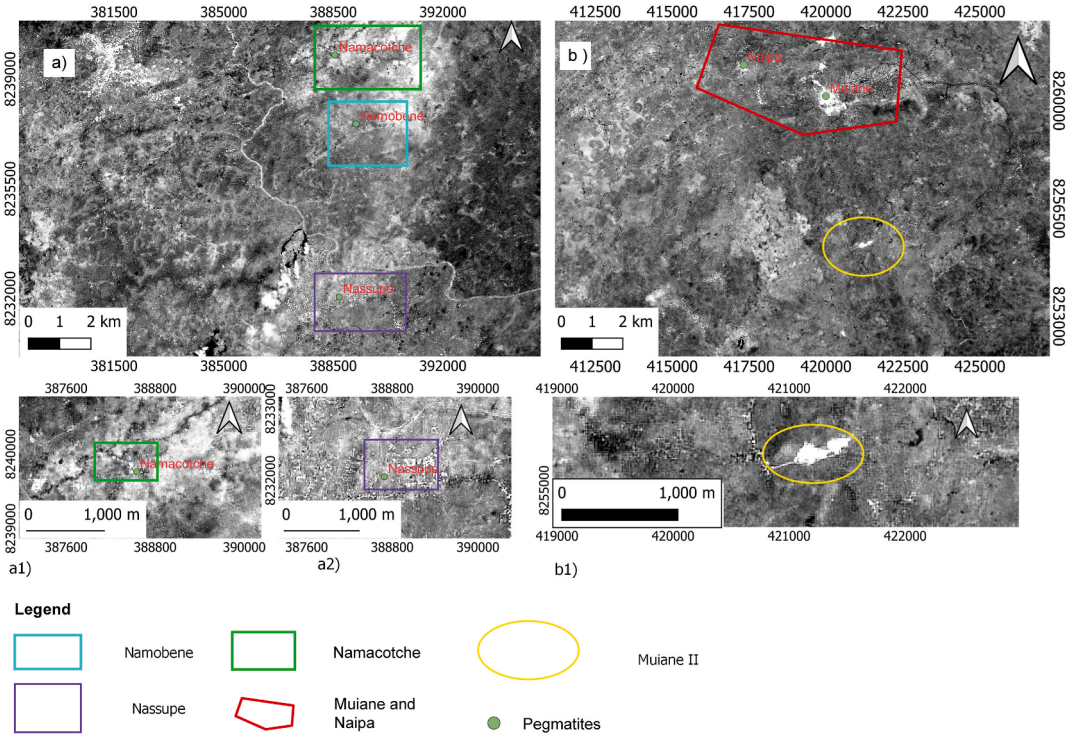

Fig. 6. Mosaic result of selective PCA on Sentinel-2 bands 2, 8 A, 11, and 12, highlighting areas where hydrothermal alteration minerals, such as clays, may occur. The presence of these minerals is evident in Muiane and Naipa (b) and Muiane II (b1).

The results obtained confirm the potential of remote sensing data and techniques not only for the detection of pegmatites, but also that the methodology proposed by Cardoso-Fernandes et al. (2019) for Li-pegmatite detection in Iberia, considering the available reference spectra of Li-bearing minerals (such as spodumene and lepidolite), also works to delimit new Li-pegmatite prospect areas in regions with characteristics (namely climate, mineralogy of pegmatite, and overall geological context). Nonetheless, the self-proposed methods are also successful in pegmatite identification.

5.2. RGB band combinations

Different false-color band combinations highlight many features ranging from mineralogical changes to moisture changes, etc. (Ghulam et al., 2010). In this study, the self-proposed RGB combination (3-11-12) was able to highlight the target areas of Muiane and Naipa in yellowish colors (Fig. 7). A similar color is observed near the greenfield area of Nassupe.

Moreover, the RGB combination (3-2-12) to better identify Li-bearing pegmatites was used for comparison (Fig. 8). Overall, the results were satisfactory since this combination not only allows identifying the known target areas (brownfields) of Muiane and Naipa (a1) but also highlights greenfield pegmatite areas in the Alto Ligonha region, such as Namobene (a3) and Muiane II (b1). Comparing the three combinations, similar results are obtained for the target areas, but the one that allowed the identification of more greenfield pegmatites was the RGB combination (3-2-12).

5.3. Band ratios

Among the self-proposed ratios, only two presented satisfactory results in both training and validation areas. Fig. 9 respects to ratio 2/11 which highlights in bright pixels the areas of Muiane (b), Muiane II (b1), Namacotche (a1), and Nassupe (a2). Nonetheless, there is a large area West of Muiane II with bright pixels indicating some spectral confusion, while the signal from Muiane II is faint when compared with other methods (Fig. 9).

Although band ratio 7/11 can identify pegmatite occurrences (Fig. 10), it shows the worst performance when compared with ratio 2/11, highlighting the areas of Muiane (b), and Muiane II (b1) as well as Namacotche (a1) in slightly less bright pixels. In this case, there is a spectral similarity between the pegmatites and water lines/bodies.

Compared with other ratios proposed in the literature such as 3/8 (Cardoso-Fernandes et al., 2019), there is a similar performance in the Muiane and Muiane II sites: a worst performance in the Nassupe validation area, and better performance in the Namacotche site. This could be due to distinct spectral signatures and mineral assemblages of the pegmatites, with certain ratios highlighting distinct areas. Therefore, a combination of several approaches should be considered to obtain the maximum of possible interest areas for further exploration.

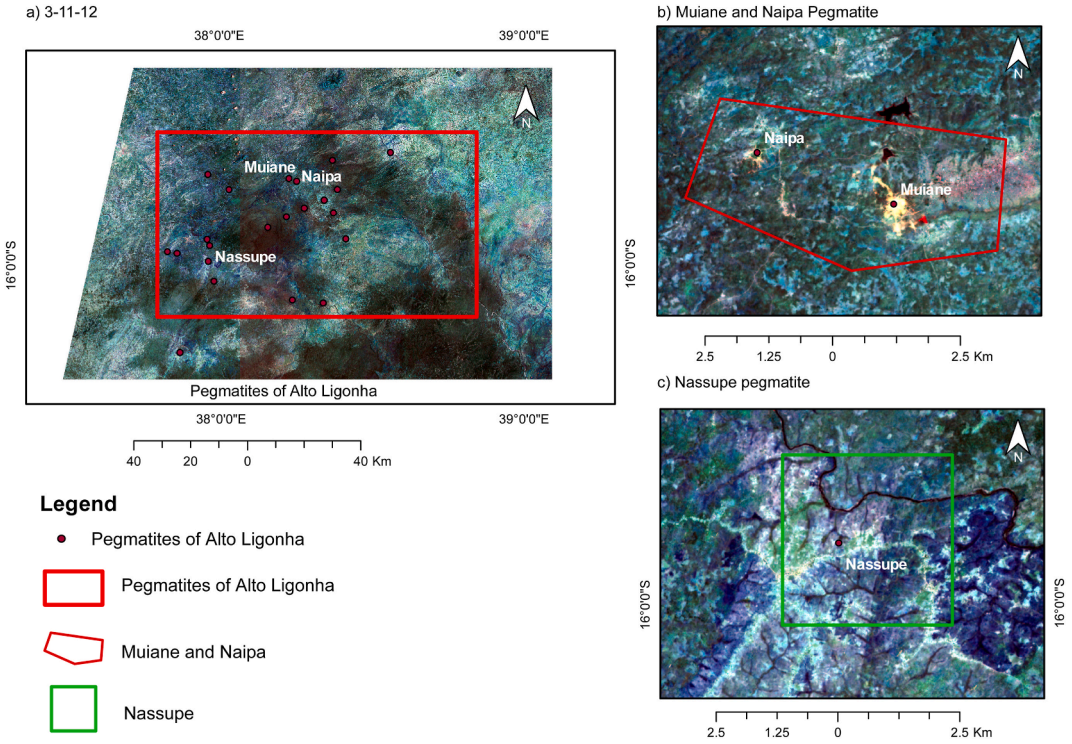

Fig. 7. Self-proposed RGB combination 3-11-12 of the Sentinel-2 image highlighting the target areas of Muiane and Naipa in yellowish colors, as well as the greenfield area of Nassupe. (For interpretation of the references to color in this figure legend, the reader is referred to the Web version of this article.)

5.4. Supervised classification

The SVM classification algorithm was applied to obtain the land cover classification map from the Sentinel-2A satellite image (Fig. 11-a). In this study, from a total of 5283 training pixels, 933 out of 946 pixels were classified as pegmatites, 414 out of 414 pixels as water bodies, 1034 out of 1047 pixels as bare soils and built-up, and 2873 out of 2873 pixels were classed as forest.

Additionally, different metrics can be used to compare different classifiers from different matrices and to determine whether one result is significantly better than another (Congalton and Green 2009; Sokolova and Lapalme 2009). The classification accuracy statistics are summarized in Tables 3 and 4 as well as in Tables A1-A2 (Appendix A). The overall accuracy (OA) of the SVM classification was (5254/5283) 99.45%, and the Kappa value (statistics) was 0.99. For the MLC technique (Fig. 11-b), the Kappa value and OA achieved were, respectively, 0.98 and 98.7% (Tables 3 and 4).

Nonetheless, recent studies point out the weakness of Kappa statistics for remote sensing classification, leading to misleading results (Foody 2020). Thus, other metrics should also be evaluated. The PA and UA of the pegmatite, waterbody, bare and built-up soils, and forest classes of the two algorithms are shown in Tables 3 and 4 Comparing Fig. 11 a and b, it is clear that: (i) SVM outperformed MLC in the classification of "bare soils and built-up" which is in accordance with the UA (Tables 3 and 4); (ii) although both algorithms correctly identify the "water bodies" of the region, SVM overestimates this class which may indicate overfitting of the algorithm in this class (corroborated by Table 3); (iii) on the contrary, MLC overestimates the occurrence of "pegmatites" when compared with SVM, despite the higher UA (Table 4), with both showing spectral confusion with "bare soils and built-up". However, Table 4 shows that MLC presents a lower UA (higher commission error) for the "bare soils and built-up" when compared with SVM (Table 3). In general, both algorithms show similar precision, but SVM presents a better sensitivity/recall and a lower FPR, while MLC has a lower FNP. This means that SVM minimizes missing possible target pegmatite areas, while MLC prioritizes avoiding misclassification. In mineral exploration, the first scenario is usually preferred so that any potential areas are not missed in field campaigns. Despite this, both algorithms were able to identify the target areas of Muiane and Naipa and to define possible prospect areas.

Numerous studies compare the results of the SVM and MLC algorithms, for example, (Mondal et al., 2012; Deilmai et al., 2014). Overall, these studies show that the SVM classification method provides better results than the MLC technique. Similarly, in this work, SVM had a better performance in pegmatite classification. Moreover, SVM was recently employed to identify Li-bearing pegmatites in the Iberian Peninsula (Cardoso-Fernandes et al., 2020b). The results showed that it is crucial to account for class imbalance, i.e., a smaller number of training pixels for the pegmatite class in comparison with other classes. This is due to the small size of the exposition of pegmatites compared to the spatial resolution of free sensors (Cardoso-Fernandes et al., 2020a, 2020b). Unfortunately, transfer learning for remote sensing image classification is not a reality yet (Li et al., 2018). That is why, is it important to fine-tune the SVM of the hyperparameters for each area, due to its particular specifications and characteristics.

In this study, it was possible to establish that the precise characterization of pegmatite targets requires a good spatial resolution, such as the one attained in the Sentinel-2 image or higher. The addition of a high spectral resolution combined with the existing ade-

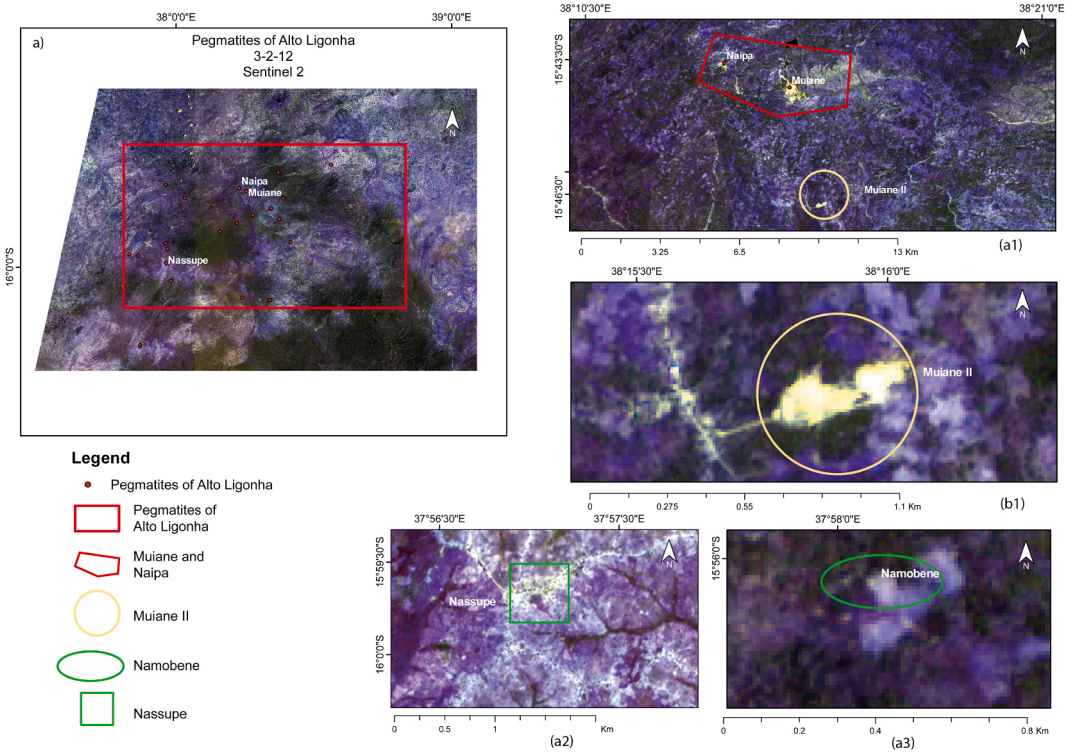

Fig. 8. RGB combination 3-2-12 of the Sentinel-2 image highlighting the greenfield pegmatite areas of Muiane II (b1) and Namobene (a3), as well as the target areas of Muiane and Naipa (a1) in yellowish pixels. Similar colors are observed near the validation area of Nassupe. (For interpretation of the references to color in this figure legend, the reader is referred to the Web version of this article.)

quate spatial resolution can lead to a more detailed and accurate detection of pegmatites in the work area, especially in greenfield zones. For example, the higher spectral resolution of ASTER, specially designed for geological applications, can be combined with the Sentinel-2 spatial resolution through various image fusion techniques (Mezned et al., 2010; Abrams and Yamaguchi 2019).

5.5. Validation of the results

As mentioned before, field validation not only allowed to corroborate the discovery of new pegmatite bodies, but the analysis of spectra of the samples collected in the field also allowed for validation of the adequacy of the methods self-proposed. For example, Fig. 12-a shows the spectra of kunzite (spodumene gem) from the Naipa training site. Most absorption features are within the VNIR region and should be due to impurities in the mineral structure of iron or manganese (Clark et al., 1993). When comparing with the positions of the Sentinel-2 bands, and considering highly reflective areas and low reflective areas, all self-proposed ratios (2/11, 7/11, 8/11) could be used to detect kunzite. Nonetheless, the signals around the Naipa pegmatite are not the most pronounced in Figs. 9 and 11. This could be due to the relation between the size of the minerals and the spectral resolution of the sensor and also the own spatial resolution of the satellite sensor that can produce spectral mixing at the pixel level. It is also noteworthy, that the reflectance magnitude is low with the bands of the RGB composition 3-11-12.

Fig. 12-b represents the muscovite from Muiane. Typical white mica features are observed, namely a sharp OH band at 1405 nm, absence of pronounced water feature, sharp and symmetric main AlOH feature at 2201 nm, and associated AlOH secondaries at 2351 nm and 2448 nm (Hunt and Ashley 1979; Pontual et al., 2008). Although the OH and water bands are at the edge or outside the atmospheric windows, they are crucial for the identification of spectrally active minerals such as white mica. Moreover, iron absorptions in VNIR at 862 nm and 1196 nm are visible. The first iron absorption associated with a reflectance peak around 733 nm indicates the presence of hematite (Hunt and Ashley 1979; Pontual et al., 2008). In such cases, the band ratio 7/11 could be useful. PCA on bands 4,6. Could also be sensitive to the presence of goethite.

In the case of Fig. 12-c, the spectrum of potassium feldspar from Muiane is represented. The main absorption features indicate alteration to a kandite group mineral, possibly halloysite due to the inflections in the OH and AlOH features as well as the pronounced water feature at 1910 nm (Pontual et al., 2008). A small inflection is also present within the width of band 4. The reflectance magnitude is high and stable between bands 6 and 8, high in band 11, and low within band 12. This indicates that both ratios 8/12, PCA on bands 4,6, and RGB 3-11-12 could be sensitive to this spectral signature.

Finally, Fig. 12-d represents a spectrum from a lepidolite sample from Muiane. The same diagnostic features of white mica in Fig. 12-b are visible, but the two are discriminated by the peak in the red region (band 4) of lepidolite. In this case, lepidolite is highly reflective in band 4, with reflectance dropping in band 6, validating the usefulness of PCA in bands 4 and 6. Moreover, lepidolite has low reflectance in band 3, high reflectance in band 11, and the lowest reflectance magnitude in band 12.

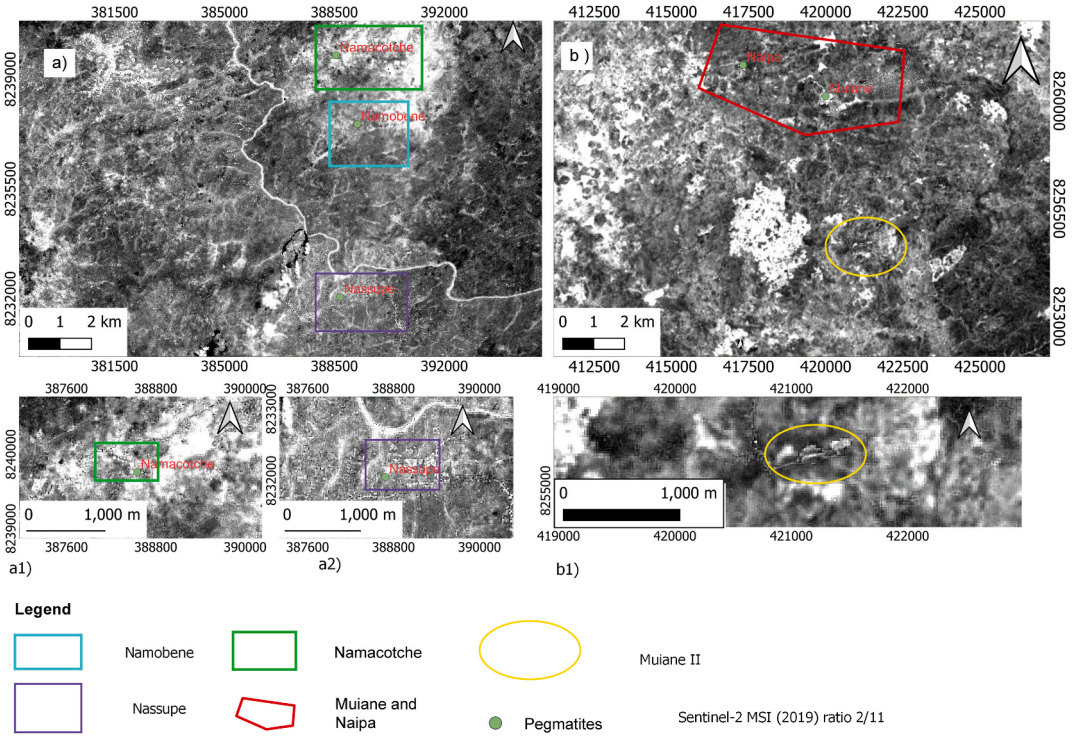

Fig. 9. Self-proposed 2/11 ratio for the Sentinel-2 image showing in bright pixels the target area of Muiane (b) and the greenfield areas of Muiane II (b1), Namacotche (a1), and Nassupe (a2).

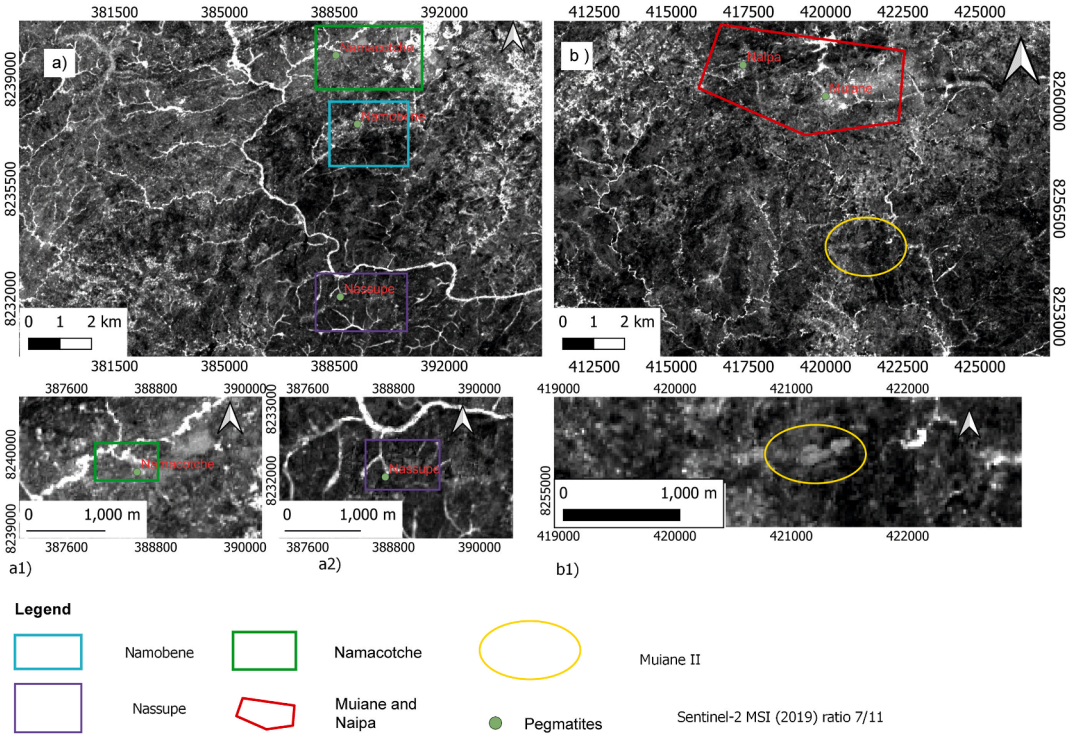

Fig. 10. Self-proposed 7/11 ratio for the Sentinel-2 image highlighting in bright pixels the area of Muiane (b), and in intense grey pixels the sites of Muiane II (b1) and Namacotche (a1).

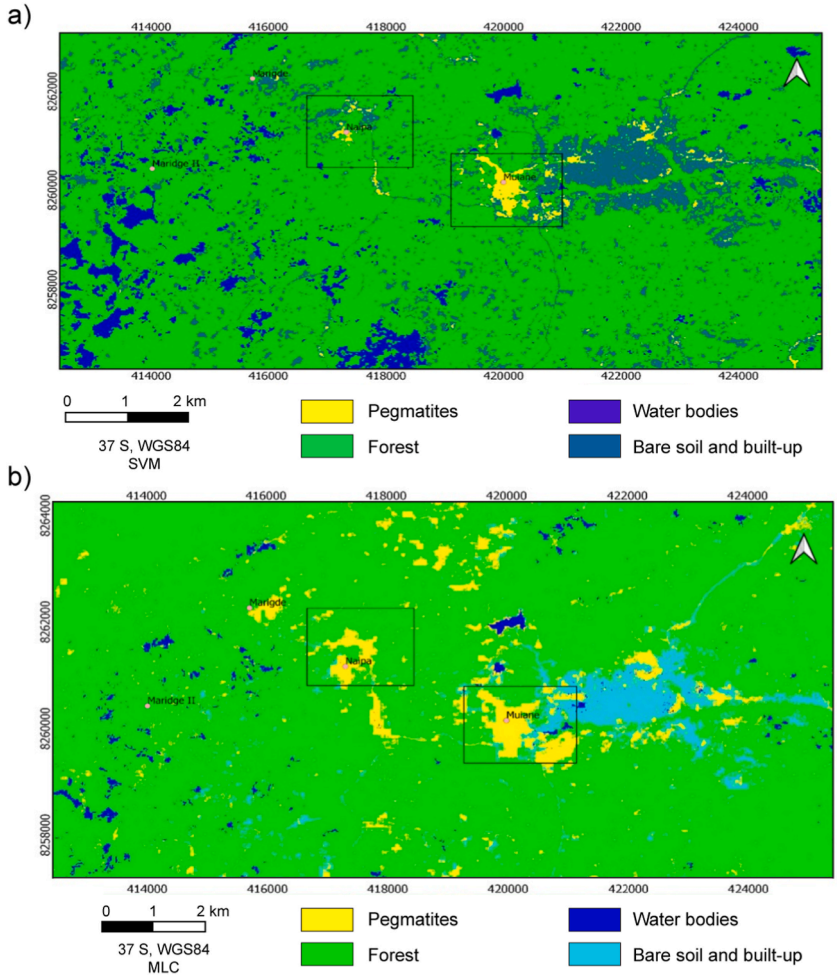

Fig. 11. Land cover classification maps of the study area in 2019 using Sentinel-2A imagery, generated with SVM (a) and MLC algorithms (b).

Table 3
Evaluation metrics for multi-class classification using SVM, according to Sokolova and Lapalme (2009). PA – producer's accuracy; UA – user's accuracy; TPR – true positive rate; FPR – false positive rate; FNR – false negative rate.

	Accuracy	PA	UA	Precision	Recall/Sensitivity/TPR	F-score	FPR	Specificity	FNR
Pegmatites	0.9955	0.9863	0.9915	0.9915	0.9831	0.9873	0.0018	0.9982	0.6667
Water bodies	1	1	1	1	1	1	0	1	0
Bare soils and built up	0.9945	0.9876	0.9848	0.9848	0.9876	0.9862	0.0038	0.9962	0.4483
Forest	0.9990	1	0.9983	0.9983	1	0.9991	0.0021	0.9979	0
Micro average	0.9945			0.9945	0.9945	0.9945	0.0018	0.9982	0.5000
Macro average	0.9973			0.9936	0.9927	0.9932	0.0019	0.9981	0.2787

Table 4
Evaluation metrics for multi-class classification using MLC, according to Sokolova and Lapalme (2009). PA – producer's accuracy; UA – user's accuracy; TPR – true positive rate; FPR – false positive rate; FNR – false negative rate.

	Accuracy	PA	UA	Precision	Recall/Sensitivity/TPR	F-score	FPR	Specificity	FNR
Pegmatites	0.9955	1	0.9934	0.9934	1	0.9967	0.0025	0.9975	0.0000
Water bodies	1	0.8834	0.9855	1	0.8834	1	0.0011	0.9989	0
Bare soils and built up	0.9945	0.9891	0.9554	0.9554	0.9891	0.9720	0.0130	0.9870	0.1905
Forest	0.9990	0.9963	1	1	0.9963	0.9982	0	1	1
Micro average	0.9871			0.9871	0.9871	0.9871	0.0043	0.9957	0.5000
Macro average	0.9935			0.9836	0.9672	0.9932	0.0041	0.9959	0.2976

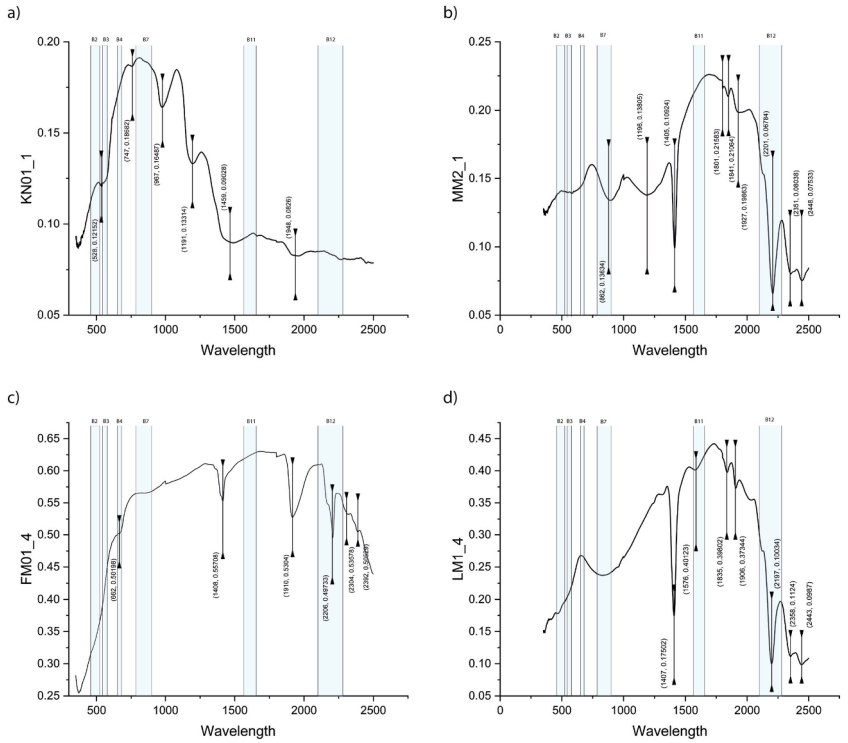

Fig. 12. Laboratory reflectance spectra of representative samples collected during field validation: (a) kunzite from Naipa; (b) muscovite from Muiane; (c) potash feldspar from Muiane; (d) lepidolite from Muiane. Selected Sentinel-2 bands are overlaid over the spectra. Red edge, aerosol, water vapor, and cirrus bands were omitted for readability purposes. (For interpretation of the references to color in this figure legend, the reader is referred to the Web version of this article.)

Overall, by superposing the Sentinel-2 bands over the reference spectra, it is possible to see that a higher spectral resolution, especially in the SWIR region, would increase the capability to identify pegmatites. This spectral limitation is in line with the interpretation of the results obtained through Sentinel-2 image processing.

6. Conclusions

- This study explored remote sensing techniques, such as RGB combinations, band ratios, selective PCA, and image classification algorithms, specifically SVM and MLC algorithms, for pegmatite exploration in the Alto Ligonha region in Mozambique, where the brownfield areas of Muiane and Naipa can be found.
- Regarding the PCA technique, the correct selection of bands for selective PCA resulted in high efficiency not only in the identification of brownfield regions such as Muiane and Naipa, but also of the greenfield areas of Namobene, Nassupe, and Muiane II (a new pegmatite target was identified through remote sensing where an unexploited and previously unmapped pegmatite containing lepidolite and spodumene gems was observed in the field validation campaigns).
- The RGB combination technique allowed identifying target areas for the occurrence of pegmatites through the comparison of the results obtained with the ones described in the literature. These prospects correspond to the known target areas of Muiane and Naipa, and new greenfield areas were also identified with PCA. The self-proposed band ratios slightly outperformed the self-proposed RGB combination.
- Considering the supervised classification, the level of accuracy is comparatively better in the SVM compared to that with the MLC method. The regional differences obtained between these two methods are comparatively smaller, with one algorithm performing better for a given class and vice-versa. Nonetheless, these two methodologies allowed the detection of the known pegmatites of Muiane and Naipa and identify possible prospective areas of interest.
- The visible and near-infrared (VNIR) and shortwave infrared (SWIR) bands of Sentinel-2 images can detect spectral features of distinct pegmatite minerals, and with their high spatial resolution, can provide a great advantage in geological exploration studies in areas with difficult access, as is the case of the Alto the Ligonha region.
- Overall, the main advantages of the methods proposed for Sentinel-2 data rely on the low cost, coverage of large areas (some with low or inexistent access), and relatively quick results that can identify outcropping pegmatites and pinpoint areas of interest for future exploration. Nonetheless, there are some limitations regarding the spatial resolution, since some smaller pegmatite dykes may only be detected using very high-resolution data such as Worldview 3 data. By comparing with the laboratory spectra, the number of available bands is another constraint, because pegmatite identification can benefit from a higher number of bands in the SWIR region. These smaller pegmatite dykes can be detected in the future, considering higher spatial and spectral satellite resolution data.

- The obtained results and the self-proposed algorithms are of great importance since they can help to better elucidate the economic interest of the Alto de Ligonha region and may lead to further development in these areas.
- Future research may include the application of other machine learning algorithms such as random forest or neural networks as well as the integration of Sentinel-2 with radar (Sentinel-1) and/or LiDAR data.

Ethical statement for Remote Sensing Applications: Society and Environment

I testify on behalf of all co-authors that our article submitted to Remote Sensing Applications: Society and Environment.
All authors: Ubaldo Gemusse. Joana Cardoso-Fernandes, Alexandre Lima, Ana Teodoro.

1) this material has not been published in whole or in part elsewhere;
2) the manuscript is not currently being considered for publication in another journal;
3) all authors have been personally and actively involved in substantive work leading to the manuscript, and will hold themselves jointly and individually responsible for its content.

Declaration of competing interest

The authors declare that they have no known competing financial interests or personal relationships that could have appeared to influence the work reported in this paper.

Data availability

Data will be made available on request.

Acknowledgments

The authors would like to thank the European Space Agency (ESA) and the American Geological Survey (USGS) for free access to the multispectral images used. The work was supported by National Funds through the FCT – Fundação para a Ciência e a Tecnologia, I.P., projects UIDB/04683/2020 and UIDP/04683/2020 - ICT (Institute of Earth Sciences). Ubaldo Gemusse is financially supported by a Ph.D. Thesis, ref. D101/2016–2018, finnaced by the Instituto de Bolsas de Moçambique (IBE). Joana Cardoso-Fernandes was financially supported within the compass of a Ph.D. Thesis, ref. SFRH/BD/136108/2018, by national funds from MCTES through FCT, and co-financed by the European Social Fund (ESF) through POCH – Programa Operacional Capital Humano – and NORTE 2020 regional program. The authors thank Douglas Santos for the help with the spectroradiometric measurements.

Appendix A

Table A1
Error matrix for SVM classification result in the study area (Ground Truth, Percent).

Class	Ground Truth (Percent)				
	Pegmatites	Waterbody	Bare soils and built up	Forest	Total
Unclassified	0.00	0.00	0.00	0.00	0.00
Pegmatites	98.31	0.00	0.76	0.00	17.81
Waterbody	0.00	100.00	0.00	0.00	7.84
Bare soils and built up	1.69	0.00	98.76	0.00	19.88
Forest	0	0	0.48	100.00	54.48
Total	100.00	100.00	100.00	100.00	100.00

Table A2
Error matrix for Maximum Likelihood classification result in the study area (Ground Truth (Percent).

Class	Ground Truth (Percent)				
	Pegmatites	Waterbody	Bare soils and built up	Forest	Total
Unclassified	0.00	0.00	0.00	0.00	0.00
Pegmatites	100.00	0.26	0.63	0.05	27.33
Waterbody	0.00	88.34	0.45	0.00	6.88
Bare soils and built up	0.00	11.40	98.91	0.32	22.75
Forest	0.00	0.00	0.00	99.63	43.04
Total	100.00	100.00	100.00	100.00	100.00

References

Abdelsalam, M.G., Liégeois, J.P., Stern, R.J., 2002. The saharan metacraton. J. Afr. Earth Sci. 34, 119–136.

Abrams, M., Yamaguchi, Y., 2019. Twenty years of ASTER contributions to lithologic mapping and mineral exploration. Rem. Sens. 11, 1–27.

Adiri, Z., Lhissou, R., El, A., Jellouli, A., Chakouri, M., 2020. Recent advances in the use of public domain satellite imagery for mineral exploration : a review of Landsat-8 and Sentinel-2 applications. Ore Geol. Rev. 117, 103332.

Aqeel, M., Jamil, M., Yusoff, I., 2011. Introduction to remote sensing of biomass. Biomass Remote Sens. Biomass 43.

Barros, R., Vicente, C., 1963. Estudo dos campos pegmatiticos da Zambezia relatorio da mossão de estudos em Moçambique campanha de 1963. p. 133.

Bingen, B., Jacobs, J., Viola, G., Henderson, I.H.C., Skår, Boyd, R., Thomas, R.J., Solli, A., Key, R.M., Daudi, E.X.F., 2009. Geochronology of the Precambrian crust in the Mozambique belt in NE Mozambique, and implications for Gondwana assembly. Precambrian Res. 170, 231–255.

Blokoi, M., Poormirzaee, R., 2009. Using ASTER image processing for hydrothermal alteration and key alteration minerals mapping. Int. J. Geol. 3, 38–43.

Booysen, R., Lorenz, S., Thiele, S.T., Fuchsloch, W.C., Marais, T., Nex, P.A.M., Gloaguen, R., 2022. Accurate hyperspectral imaging of mineralised outcrops: an example from lithium-bearing pegmatites at Uis, Namibia. Remote Sens. Environ. 269, 112790. https://doi.org/10.1016/j.rse.2021.112790.

Boyd, R., Nordgulen, Thomas, R.J., Bingen, B., Bjerkgård, T., Grenne, T., Henderson, I., Melezhik, V.A., Often, M., Sandstad, J.S., others, 2010. The geology and geochemistry of the East African orogen in northeastern Mozambique. S. Afr. J. Geol. 113, 87–129.

Bradley, D.C., McCauley, A., 2016. A Preliminary Deposit Model for Lithium-Cesium-Tantalum (LCT) Pegmatites, pp. 1–7. USGS Open File Report.

Bradley, D.C., McCauley, A.D., Stillings, L.M., 2010. Mineral-Deposit Model for Lithium-Cesium- Tantalum Pegmatites Mineral Deposit Models for Resource Assessment Scientific Investigations Report 2010–5070–O.

Cardoso-Fernandes, J., Teodoro, A.C., Lima, A., 2019. Remote sensing data in lithium (Li) exploration: a new approach for the detection of Li-bearing pegmatites. Int. J. Appl. Earth Obs. Geoinf. 76, 10–25.

Cardoso-Fernandes, J., Teodoro, A.C., Lima, A., Perrotta, M., Roda-Robles, E., 2020a. Detecting lithium (Li) mineralizations from Space: current research and future perspectives. 2020. Appl. Sci. 10, 1785. . 10, 1785.

Cardoso-Fernandes, J., Teodoro, A.C., Lima, A., 2020b. Semi-automatization of support vector machines to map lithium (Li) bearing pegmatites. 2020. Rem. Sens. 12, 2319.

Cardoso-Fernandes, J., Silva, J., Dias, F., Lima, A., Teodoro, A.C., Barrès, O., Cauzid, J., Perrotta, M., Roda-Robles, E., Ribeiro, M.A., 2021a. Tools for remote exploration: a lithium (Li) dedicated spectral library of the fregeneda–almendra aplite–pegmatite field. Data 6 (3), 33. https://doi.org/10.3390/data6030033.

Cardoso-Fernandes, J., Silva, J., Perrotta, M.M., Lima, A., Teodoro, A.C., Ribeiro, M.A., Dias, F., Barrès, O., Cauzid, J., Roda-Robles, E., 2021b. Interpretation of the reflectance spectra of lithium (Li) minerals and pegmatites: a case study for mineralogical and lithological identification in the fregeneda–almendra area. Rem. Sens. 13 (18), 3688. https://doi.org/10.3390/rs13183688.

Chavez, P.S., 1996. Image-based atmospheric corrections - revisited and improved. Photogramm. Eng. Rem. Sens. 62, 1025–1036.

Černý, P., Ercit, T.S., 2005. The classification of granitic pegmatites revisited. Can. Mineral. 43, 2005–2026.

Chaudhari, N.S., Tiwari, A., Thomas, J., 2015. Support vector machine based semi-supervised classification. Int. J. Comput. Sci. Syst. Anal. 3, 10.

Chen, L., Jin, X., Chen, H., He, Z., Qiu, L., Duan, H., 2020. Grain size distribution and clay mineral distinction of rare earth ore through different methods. Minerals 10, 1–27.

Clark, R.N., Swayze, G.A., Gallagher, A.J., King, T.V.V., Calvin, W.M., 1993. The U. S. Geological Survey, Digital Spectral Library: Version 1 (0.2 to 3.0um), Open-File Report.

Congalton, R., Green, K., 2009. In: L. Taylor & Francis Group (Ed.), Assessing the Accuracy of Remotely Sensed Data: Principles and Practices. second ed. The Photogrammetric Record, vol. 25, p. 210.

Congalton, R.G., 1991. A review of assessing the accuracy of classifications of remotely sensed data. Remote Sens. Environ. 37, 35–46.

Congedo, L., 2016. Semi-Automatic Classification Plugin Documentation. https://doi.org/10.13140/RG.2.2.29474.02242/1. Retrieved from.

Corumluoglu, O., Vural, A., Asri, I., 2015. Determination of Kula basalts (geosite) in Turkey using remote sensing techniques. Arabian J. Geosci. 8, 10105–10117.

Çorumluoğlu, O., Vural, A., 2013. PCA of Landsat band ratio images for capturing kula basalts in Turkey. In: Proceedings of the Second International Conference on Water, Energy and the Environment. Kusadası, Turkey, p. 651.

Council for Geoscience, 2007. Map Explanation: Sheets 1537 Alto Molócuè, 1538 Murrupula, 1539 Nampula, 1540 Mogincual, 1637 Errego, 1638 Gilé and 1639–40 Angoche, Ministério dos Recuursos Minerais e Energia. Mozambique and Council for Geoscience, Pretoria, South Africa, Maputo.

Cronwright, M.S.C., 2005. A Review of the Rare-Element Pegmatite's of the Alto Ligonha Pegmatite Province, Northern Mozambique. vol. 2005.

Cŕosta, A.P., De Souza Filho, C.R., Azevedo, F., Brodie, C., 2003. Targeting key alteration minerals in epithermal deposits in Patagonia, Argentina, using ASTER imagery and principal component analysis. Int. J. Rem. Sens. 24, 4233–4240.

De Luca, G., M. N. Silva, J., Di Fazio, S., Modica, G., 2022. Integrated use of Sentinel-1 and Sentinel-2 data and open-source machine learning algorithms for land cover mapping in a Mediterranean region. Eur. J. Remote Sens. 55 (1), 52–70. https://doi.org/10.1080/22797254.2021.2018667.

Deilmai, B., Ahmad, B., Zabihi, H., 2014. Comparison of two classification methods (MLC and SVM) to extract land use and land cover in Johor Malaysia. 7th IGRSM Int. Remote Sens. GIS Conf. Exhib. 20, 7.

Delacourt, C., Allemand, P., Ledru, P., Wackerle, R., 2005. Using ASTER remote sensing data set for geological mapping. Namibia 30, 97–108.

Didero, J., Wambo, T., Beiranvand, A., Ganno, S., Asimow, P.D., Zoheir, B., Salles, R., Paul, J., Pradhan, B., Muslim, A.M., 2020. Identifying high potential zones of gold mineralization in a sub-tropical region using Landsat-8 and ASTER remote sensing data : a case study of the Ngoura-Colomines goldfield, eastern Cameroon. Ore Geol. Rev. 122, 103530.

Dolui, G., Chatterjee, S., Das Chatterjee, N., 2016. Geophysical and geochemical alteration of rocks in granitic profiles during intense weathering in southern Purulia district, West Bengal, India. Model. Earth Syst. Environ. 2, 1–22.

El-leil, I.A., Mohamed, N., Soliman, A., Bekiet, M.H., 2019. Enhancing multispectral remote sensing data interpretation for historical gold mines in Egypt : a case study from Madari gold mine Enhancing multispectral remote sensing data interpretation for historical gold mines in Egypt : a case study from Madari gol. Arabian J. Geosci. 12 (3), 11.

ENVI User's Guide, 2009. ENVI on-line software user's manual, ITT visual information solutions. https://www.tetracam.com/PDFs/Rec_Cite9.pdf.

Fal, S., Maanan, M., Baidder, L., Rhinane, H., 2019. The contribution of Sentinel-2 satellite images for geological mapping in the south of Tafilalet basin (Eastern Anti-Atlas, Morocco). In: The International Archives of the Photogrammetry, Remote Sensing and Spatial Information Sciences, XLII, pp. 10–11. (Morocco).

Foody, G.M., 2020. Explaining the unsuitability of the kappa coefficient in the assessment and comparison of the accuracy of thematic maps obtained by image classification. Remote Sens. Environ. 239, 111630. https://doi.org/10.1016/j.rse.2019.111630.

Frutuoso, R., Lima, A., Teodoro, A., 2021. Application of remote sensing data in gold exploration: targeting hydrothermal alteration using Landsat 8 imagery in northern Portugal. Arabian J. Geosci. 14.

Gaspar, P., Carbonell, J., Oliveira, J.L., 2012. On the parameter optimization of Support Vector Machines for binary classification. J. Integrat. BioInfo. 9, 201.

Gemusse, U., Lima, A., Teodoro, A., 2018. Pegmatite spectral behavior considering ASTER and Landsat 8 OLI data in Naipa and Muiane mines (Alto Ligonha, Mozambique). In: Earth Resources and Environmental Remote Sensing/GIS Applications IX. p. 11. (Berlin, Germany).

Gemusse, U., Lima, A., Teodoro, A.C.M., 2019. Comparing different techniques of satellite imagery classification to mineral mapping pegmatite of Muiane and Naipa: Mozambique). In: Conference-Proceedings-of-SPIE. p. 49. (Strasbourg, France).

Gemusse, U., Shaik, S., Uachave, B.F., 2021. Plano da Mina e Vendas para 2022, Mina de Muiane, Distrito do Gilé, Província da Zambézia [report]. Tantalum Mineração e Prospecção Limitada 24.

Ghulam, A., Amer, R., Kusky, T.M., 2010. Mineral exploration and alteration zone mapping in Eastern Desert of Egypt using aster data. Am. Soc. Photogramm. Remote Sens. Annu. Conf. 2010: Opportun. Emerg. Geospatial Technol. 1, 196–205.

Gomes, C.L., 2003. O papel dos fenómenos de evolução tardia na génese de gemas pegmatíticas - ilações da análise paragenética em pegmatitos LCT do Alto Ligonha (Moçambique). In: A Geologia e os Recursos Geológicos. Coimbra, Imprensa da Universidade, v. II. pp. 217–228.

Gomes, C.L., Marques, J., Dias, P., Costa, J., 2008. Análise descritiva das Unidades Portadoras de Mineralização Tantalífera em Pegmatitos do Sul da Província

Zambeziana (Moçambique). In: 2° Congresso de Engenharia de Moçambique. Universidade do Minho, Maputo, p. 23.
Gonzalez-Abril, L., Nuñez, H., Angulo, C., Velasco, F., 2014. GSVM: an SVM for handling imbalanced accuracy between classes inbi-classification problems. Appl. Soft Comput. 17, 23–31.
Gopinathan, P., Parthiban, S., Magendran, T., Al-quraishi, A.M.F., Singh, A.K., 2020. Mapping of ferric (Fe3 +) and ferrous (Fe2 +) iron oxides distribution using band ratio techniques with ASTER data and geochemistry of Kanjamalai and Godumalai , Tamil Nadu, south Ind .Remote Sensing Applications : Society and Environment Mapping. Remote Sens. Appl.: Soc. Environ. 18, 100306.
Govil, H., Tripathi, M.K., Diwan, P., Guha, S., 2018. Identification of iron oxides minerals in western jahajpur region, India using aviris-ng hyperspectral remote sensing. Int. Arch. Photogram. Rem. Sens. Spatial Inf. Sci. XLII, 20–23.
Grebby, S., Cunningham, D., Tansey, K., Naden, J., 2014. The impact of vegetation on lithological mapping using airborne multispectral data: a case study for the north troodos region, Cyprus. Rem. Sens. 6 (11), 10860–10887. https://doi.org/10.3390/rs61110860.
Hassan, S.M., Ramadan, T.M., 2015. Mapping of the late Neoproterozoic Basement rocks and detection of the gold-bearing alteration zones at Abu Marawat-Semna area, Eastern Desert, Egypt using remote sensing data. Arabian J. Geosci. 8, 4641–4656.
Hu, B., Xu, Y., Wan, B., Wu, X., Yi, G., 2018. Hydrothermally altered mineral mapping using synthetic application of Sentinel-2A MSI, ASTER and Hyperion data in the Duolong area, Tibetan Plateau, China. Ore Geol. Rev. 101, 384–397.
Huang, C., Davis, L.S., Townshend, J.R.G., 2002. An assessment of support vector machines for land cover classication. Int. J. Rem. Sens. 23, 725–749. . Article in.
Hunt, G.R., Ashley, R.P., 1979. Spectra of altered rocks in the visible and near infrared. Econ. Geol. 74, 1613–1629.
Jacobs, Joachim, Thomas, B., Ueda, K., Jacobs, J., Thomas, R.J., Kosler, J., Jourdan, F., Matola, R., 2012. Delamination-induced late-tectonic deformation and high-grade metamorphism of the Proterozoic Nampula Complex, northern Mozambique Delamination-induced late-tectonic deformation and high-grade metamorphism of the Proterozoic Nampula Complex, northern Mo. Precambrian Res. 196–197, 275–294.
Jensen, J., 2009. Remote Sensing of the Environment: an Earth Resource Perspective. São José dos Campos, p. 598.
Jia, K., Wei, X., Gu, X., Yao, Y., Xie, X., Li, B., 2014. Land cover classification using Landsat 8 operational land imager data in beijing, China. Geocarto Int. 29, 941–951.
Jolie, E., Hutchison, W., Driba, D.L., Jentsch, A., Gizaw, B., 2019. Pinpointing deep geothermal upflow in zones of complex tectono-volcanic degassing: new insights from aluto volcano, main Ethiopian rift. G-cubed 20, 4146–4161.
Khan, S., Naseem, I., Togneri, R., Bennamoun, M., 2017. A novel adaptive kernel for the RBF neural networks. Circ. Syst. Signal Process. 36, 1639–1653.
Lewes, G.H., 2015. Support vector machines for classification. In: Science Is the Systematic Classification of Experience. p. 29.
Li, Y., Zhang, H., Xue, X., Jiang, Y., Shen, Q., 2018. Deep learning for remote sensing image classification: a survey. Wiley Interdiscipl. Rev.: Data Min. Knowl. Discov. 8, e1264.
Lillesand, T.M., Kiefer, R., Chipman, J., 2015. Remote sensing and image interpretation. In: Photogrammetric Engineering & Remote Sensing, vol. 81. John Wiley & Sons, pp. 615–616.
Long, X., Li, N., Tie, X., Cao, J., Zhao, S., Huang, R., Zhao, M., Li, G., Feng, T., 2016. Urban dust in the Guanzhong Basin of China, part I: a regional distribution of dust sources retrieved using satellite data. Sci. Total Environ. 541, 1603–1613.
Loughlin, P., 1991. Principal component analysis for alteration mapping. Photogramm. Eng. Rem. Sens. 57, 1163–1169.
Lu, D., Mausel, P., Brondízio, E., Moran, E., 2004. Change detection techniques. Int. J. Rem. Sens. 25, 2365–2401.
Macey, P.H., Miller, J., Rowe, C., Grantham, G., Siegfried, P., Armstrong, R., Kemp, J., Bacalau, J., 2006. A new lithostratigraphic subdivision of the rocks of the Monapo Structure, NE Mozambique'. Precambrian Research, Abstract. 21st Colloquium Afr. Geol. 105–106.
MAE, 2005. Perfil do Distrito de Gilé, Província da Zambézia, p. 60. (Gilé).
Mahboob, M.A., Genc, B., Celik, T., Ali, S., Atif, I., 2019. Mapping hydrothermal minerals using remotely sensed reflectance spectroscopy data from Landsat. J. S. Afr. Inst. Min. Metall 119, 279–289.
Manuel, R., Brito, M., Chichorro, M., Rosa, C., 2017. Remote sensing for mineral exploration in Central Portugal. Minerals 7, 30.
Martins, S., Bernardo, N., Ogashawara, I., Alcantara, E., 2016. Support vector machine algorithm optimal parameterization for change detection mapping in funil hydroelectric reservoir (Rio de Janeiro state, Brazil). Model. Earth Syst. Environ. 2, 1–10.
Mashkoor, R., Ahmadi, H., Rahmani, A.B., Pekkan, E., 2022. Detecting Li-bearing pegmatites using geospatial technology: the case of SW konar province, eastern Afghanistan. Geocarto Int. 1–19. https://doi.org/10.1080/10106049.2022.2086633.
Maxwell, A.E., Warner, T.A., Fang, F., 2018. Implementation of machine-learning classification in remote sensing: an applied review. Int. J. Rem. Sens. 39 (9), 2784–2817. https://doi.org/10.1080/01431161.2018.1433343.
Mezned, N., Abdeljaoued, S., Boussema, M., 2010. A comparative study for unmixing based Landsat ETM + and ASTER image fusion. Int. J. Appl. Earth Obs. Geoinf. 12, 131–137.
Mondal, A., Kundu, S., Chandniha, S.K., Shukla, R., Mishra, P.K., 2012. Comparison of support vector machine and maximum likelihood classification technique using satellite imagery. J. Remote Sens. GIS 1, 116–123.
Morsli, Y., Zerhouni, Y., Maimouni, S., Alikouss, S., Kadir, H., Baroudi, Z., 2021. Pegmatite mapping using spectroradiometry and ASTER data (Zenaga, Central Anti-Atlas, Morocco). J. Afr. Earth Sci. 177, 104153. https://doi.org/10.1016/j.jafrearsci.2021.104153.
Mountrakis, G., Im, J., Ogole, C., 2011. Support vector machines in remote sensing: a review. ISPRS J. Photogrammetry Remote Sens. 66, 247–259.
Müller, A., Reimer, W., Wall, F., Williamson, B., Menuge, J., Brönner, M., Haase, C., Brauch, K., Pohl, C., Lima, A., Teodoro, A., Cardoso-Fernandes, J., Roda-Robles, E., Harrop, J., Smith, K., Wanke, D., Unterweissacher, T., Hopfner, M., Schröder, M., Clifford, B., Moutela, P., Lloret, C., Ranza, L., Rausa, A., 2022. GREENPEG - Exploration for Pegmatite Minerals to Feed the Energy Transition: First Steps towards the Green Stone Age, vol. 526. Geological Society, London, Special Publications, pp. 2021–2189. https://doi.org/10.1144/SP526-2021-189. SP526.
Naude, P., Sperinck, M., 2009. *Technical Report on the mineral Assets of tantalum Mineração and Prospecção Limitada*. 111 pp.
Neiva, A., Gomes, C.L., 2010. Geoquímica das turmalinas do grupo pegmatítico granítico Li-Cs-Ta de Naípa , Alto Ligonha, Moçambique, vol. 13. VIII Congresso Nacional de Geologia, pp. 2–5.
Neiva, A., Gomes, C.L., 2012. Tourmaline-group minerals in the Naipa Li-Cs-Ta granitic pegmatite group, Mozambique: tracers of magmatic to postmagmatic evolution trends. Neues Jahrbuch fur Mineralogie, Abhandlungen 189, 1–20.
Noi, P.T., Kappas, M., 2017. Comparison of random forest, k-nearest neighbor, and support vector machine classifiers for land cover classification using sentinel-2 imagery. Sensors 18 (1). https://doi.org/10.3390/s18010018.
Petropoulos, G.P., Kalaitzidis, C., Prasad Vadrevu, K., 2012. Support vector machines and object-based classification for obtaining land-use/cover cartography from Hyperion hyperspectral imagery. Comput. Geosci. 41, 99–107. https://doi.org/10.1016/j.cageo.2011.08.019.
Pontual, S., Merry, N.J., Gamson, P., 2008. Spectral Interpretation Field Manual. GMEX Spectral Analysis Guides for Mineral Exploration, third ed. AusSpec International Ltd., Victoria.
Pour, A., Hashim, M., 2015. Hydrothermal alteration mapping from Landsat-8 data, Sar Cheshmeh copper mining district, south-eastern Islamic Republic of Iran. J. Taibah Univ. Sci. 9, 155–166.
Quemeneur, J., Laganche, M., 1999. Comparative study of two pegmatitic fields from minas gerais , Brazil , using the Rb and Cs contents of micas and feldspars. Rev. Bras. Geociencias 29, 27–32.
Rajesh, H., 2004. Application of remote sensing and GIS in mineral resource mapping - an overview. J. Mineral. Petrol. Sci. 99, 83–103.
Rawashdeh, S. Al, Hamzah, M., 2020. The use of remote sensing technology in geological investigation and mineral detection in El azraq-Jordan. Cybergeo 1–17.
Richards, J.A., Jia, X., 1986. Remote Sensing Digital Image Analysis, fourth ed. Springer-Verlag, Berlin, Germany, p. 454.
Riley, D.N., Hecker, C.A., 2013. Mineral mapping with airborne hyperspectral thermal infrared remote sensing at cuprite, Nevada, USA. In: Kuenzer, C., Dech, S. (Eds.), Thermal Infrared Remote Sensing: Sensors, Methods, Applications. Springer Netherlands, Dordrecht, pp. 495–514.
Rodriguez-Galiano, V., Sanchez-Castillo, M., Chica-Olmo, M., Chica-Rivas, M., 2015. Machine learning predictive models for mineral prospectivity: an evaluation of neural networks, random forest, regression trees and support vector machines. Ore Geol. Rev. 71, 804–818. https://doi.org/10.1016/j.oregeorev.2015.01.001.
Sabins, F.F., 1999. Remote sensing for mineral exploration. Ore Geol. Rev. 14, 157–183.
Sadek, M.F., Hasan, S.M., Gabr, S.S., 2013. Application of aster and ETM images data in detection of gold-bearing alteration zones in south eastern desert of Egypt.

2013. 34th Asian Conf. Remote Sens. 3, 2813–2820. . ACRS 2013.
Saibi, H., Bersi, M., Mia, M., Bloush, K., 2018. Applications Applications of Remote Remote Sensing Sensing in Geoscience. p. 25.
Salehi, T., Tangestani, H.M., 2020. Evaluation of WorldView-3 VNIR and SWIR data for hydrothermal alteration mapping for mineral exploration: case study from northeastern isfahan, Iran. Nat. Resour. Res. 25.
Santos, D., Cardoso-Fernandes, J., Lima, A., Müller, A., Brönner, M., Teodoro, A.C., 2022. Spectral analysis to improve inputs to Random Forest and other boosted ensemble tree-based algorithms for detecting NYF pegmatites in Tysfjord, Norway. Rem. Sens. 14.
Santos, D., Teodoro, A., Lima, A., Cardoso-Fernandes, J., 2019. Remote Sensing Techniques to Detect Areas with Potential for Lithium Exploration in Minas Gerais, p. 50. Brazil.
Silva, S., Crosta, A., Angelica, R., Silva, H., 2009. Mineralogical characterization and mapping using reflectance spectroscopy: an experiment at Alto do giz pegmatite in the south portion of borborema pegmatite province (BPP), northeastern Brazil. Estudos Geol. 19, 337–343.
Sivakumar, M., Roy, P., Harmsen, K., S, S., 2004. Crop growth modeling and its applications in agricultural meteorology. In: Sivakumar, M., Roy, P., Harmsen, K., S. S (Eds.), Satellite remote sensing and GIS applications in agricultural meteorology. World Meteorological Organisation 7bis, Avenue de la Paix 1211 Geneva 2. p. 423. (Switzerland, Dehra Dun, India).
Sokolova, M., Lapalme, G., 2009. A systematic analysis of performance measures for classification tasks. Inf. Process. Manag. 45 (4), 427–437. https://doi.org/10.1016/j.ipm.2009.03.002.
Teodoro, A.C., Santos, D., Cardoso-Fernandes, J., Lima, A., Brönner, M., 2021. Identification of pegmatite bodies, at a province scale, using machine learning algorithms: preliminary results. 12 September 2021. In: Paper Presented at the Proc. SPIE 11863, Earth Resources and Environmental Remote Sensing/GIS Applications XII, SPIE Remote Sensing. https://doi.org/10.1117/12.2599600.
Valdivieso-Ros, C., Alonso-Sarria, F., Gomariz-Castillo, F., 2023. Effect of the synergetic use of sentinel-1, sentinel-2, LiDAR and derived data in land cover classification of a semiarid mediterranean area using machine learning algorithms. Rem. Sens. 15 (2), 312. https://doi.org/10.3390/rs15020312.
van der Meer, F.D., van der Werff, H.M.A., van Ruitenbeek, F.J.A., 2014. Potential of ESA's Sentinel-2 for geological applications. Remote Sens. Environ. 148, 124–133.
van der Werff, H., van der Meer, F., 2016. Sentinel-2A MSI and Landsat 8 OLI provide data continuity for geological remote sensing. Rem. Sens. 8, 16.
Vapnik, V.N., 2000. In: Jordan, M. (Ed.), The Nature of Statistical Learning Theory. second ed., p. 334. (New York).
Vapnik, V.N., Lerner, A., 1963. Pattern recognition using generalized portrait method. Autom. Rem. Control 24.
Xie, Y., Sha, Z., Yu, M., 2008. Remote sensing imagery in vegetation mapping: a review. J. Plant Ecol. 1, 9–23.
Yousefi, T., Aliyari, F., Abedini, A., Calagari, A.A., 2018. Integrating geologic and Landsat-8 and ASTER remote sensing data for gold exploration : a case study from Zarshuran Carlin-type gold deposit, NW Iran Integrating geologic and Landsat-8 and ASTER remote sensing data for gold exploration : a case study fro. Arabian J. Geosci. 11.
Yu, L., Liang, L., Wang, J., Zhao, Y., Cheng, Q., Hu, L., Liu, S., Yu, L., Wang, X., Zhu, P., Li, X., Xu, Y., Li, C., Fu, W., Li, X., Li, W., Liu, C., Cong, N., Zhang, H., Sun, F., Bi, X., Xin, Q., Li, D., Yan, D., Zhu, Z., Goodchild, M.F., Gong, P., 2014. Meta-discoveries from a synthesis of satellite-based land-cover mapping research. Int. J. Rem. Sens. 35 (13), 4573–4588. https://doi.org/10.1080/01431161.2014.930206.
Yu, L., Porwal, A., Holden, E.-J., Dentith, M.C., 2012. Towards automatic lithological classification from remote sensing data using support vector machines. Comput. Geosci. 45, 229–239. https://doi.org/10.1016/j.cageo.2011.11.019.